



Nuclear proliferomics: A new field of study to identify signatures of nuclear materials as demonstrated on alpha-UO₃

Ian J. Schwerdt^a, Alexandria Brenkmann^a, Sean Martinson^a, Brent D. Albrecht^b, Sean Heffernan^a, Michael R. Klosterman^a, Trenton Kirkham^a, Tolga Tasdizen^b, Luther W. McDonald IV^{a,*}

^a University of Utah, Department of Civil and Environmental Engineering, Nuclear Engineering Program, 201 Presidents Circle, Salt Lake City, UT 84112, United States

^b University of Utah, Department of Electrical and Computer Engineering, 201 Presidents Circle, Salt Lake City, UT 84112, United States

ARTICLE INFO

Keywords:

Electron microscopy
Nuclear forensics
Machine learning
Nuclear safeguards
Nuclear proliferomics
Morphology

ABSTRACT

The use of a limited set of signatures in nuclear forensics and nuclear safeguards may reduce the discriminating power for identifying unknown nuclear materials, or for verifying processing at existing facilities. Nuclear proliferomics is a proposed new field of study that advocates for the acquisition of large databases of nuclear material properties from a variety of analytical techniques. As demonstrated on a common uranium trioxide polymorph, α -UO₃, in this paper, nuclear proliferomics increases the ability to improve confidence in identifying the processing history of nuclear materials. Specifically, α -UO₃ was investigated from the calcination of unwashed uranyl peroxide at 350, 400, 450, 500, and 550 °C in air. Scanning electron microscopy (SEM) images were acquired of the surface morphology, and distinct qualitative differences are presented between unwashed and washed uranyl peroxide, as well as the calcination products from the unwashed uranyl peroxide at the investigated temperatures. Differential scanning calorimetry (DSC), UV–Vis spectrophotometry, powder X-ray diffraction (p-XRD), and thermogravimetric analysis-mass spectrometry (TGA-MS) were used to understand the source of these morphological differences as a function of calcination temperature. Additionally, the SEM images were manually segmented using Morphological Analysis for MAterials (MAMA) software to identify quantifiable differences in morphology for three different surface features present on the unwashed uranyl peroxide calcination products. No single quantifiable signature was sufficient to discern all calcination temperatures with a high degree of confidence; therefore, advanced statistical analysis was performed to allow the combination of a number of quantitative signatures, with their associated uncertainties, to allow for complete discernment by calcination history. Furthermore, machine learning was applied to the acquired SEM images to demonstrate automated discernment with at least 89% accuracy.

1. Introduction

The ability to rapidly detect and respond to a nuclear event is one of the greatest mechanisms for deterring the future use of nuclear weapons [1,2]. Nuclear forensics provides critical analysis of interdited nuclear materials and materials following detonation of a nuclear weapon to help identify signatures indicative of the materials processing history and origin [3]. On the other hand, nuclear safeguards aims to prevent the spread of nuclear weapon materials and technology through policy and treaty verification. To enable more effective safeguards and forensics, large databases of nuclear material properties are needed and Nuclear Proliferomics is the field to acquire that data. In nuclear forensics and nuclear safeguards, research is driven by the need to answer specific, hypothesis driven questions. In contrast, nuclear proliferomics research is conducted to acquire the

maximum amount of data possible. This is the same philosophy practiced in almost all fields of “omics” [4]. The investigation of these large and varied datasets can generate additional fields of research, or lead to the discovery of additional processing signatures.

At the core of almost all “omics” is mass spectrometry [4]. This technique is also critical to nuclear proliferomics for measuring isotope ratios of uranium and plutonium [5]. Nonetheless, recent advances in nuclear investigations have demonstrated the use of mass spectrometry for identifying many other key signatures including rare earth element signatures of uranium ores [6], and molecular solvent signatures of spent nuclear fuel reprocessing [7]. In addition to these mass spectrometric signatures, many other signatures can be realized from exploring the vast analytical techniques available to nuclear scientists including morphology [8], X-ray fluorescence [9], Vis/NIR reflectance spectroscopy [10], and thermal analysis [11,12]. It is a collection of all of these

* Correspondence to: University of Utah, Salt Lake City, UT 84112, United States.
E-mail address: luther.mcdonald@utah.edu (L.W. McDonald IV).

signatures which is needed for nuclear proliferomics.

Due to the size and complexity of data collected in all “omics” fields, machine learning has become a pivotal tool for processing and interpreting the data [13–15]. Nonetheless, the application of machine learning to any nuclear related research is very rare. Porter et al. has worked to develop segmentation software and interactive machine learning to interpret morphological features of nuclear materials [16,17]. In other studies, Jones et al. utilized machine learning to classify reactor type based on isotopic and elemental measurements [18], and to repurpose historical industrial quality control records from uranium ore concentrate (UOC) production to discriminate country of origin and deposit type [19]. In all of these cases, more data would greatly improve the application of machine learning. In fact, Luetzenkirchen and Mayer reported on the need of nuclear databases to aid in combatting trafficking of nuclear materials [20]. Nonetheless, extensive research in nuclear proliferomics is needed to develop these databases. As the nuclear threat continues to grow, the need for novel signatures is imperative to continue to deter nuclear material smuggling, and the use of nuclear weapons [21].

In this present study, a common uranium trioxide polymorph, α - UO_3 , was investigated from one of its many synthetic pathways. Cordfunke et al. previously discovered that unwashed uranyl peroxide results in α - UO_3 when calcined at 425 °C in air. This was in contrast to washed uranyl peroxide resulting in amorphous- UO_3 at the same temperature. The two routes resulting in drastically different morphological forms [22]. While this particular synthetic route is unlikely to be encountered in a legitimate commercial operation where the uranium oxide purity is paramount, it could result from hasty illicit production or insufficient washing during commercial processing. Furthermore, its complex chemical behavior presents an interesting case for demonstrating nuclear proliferomics. In this investigation, microstructural and morphological features of α - UO_3 were quantified using both manual particle segmentation and machine learning. Quantitative powder X-ray diffractometry (p-XRD), differential scanning calorimetry (DSC), UV–VIS spectrophotometry, and thermogravimetric analysis–mass spectrometry (TGA-MS) were used to understand why morphological features were changing based on the calcination conditions. To fully illustrate the power of nuclear proliferomics, statistical analysis was performed on a collection of the analytical data to reveal signatures not readily visible from a single analysis.

2. Experimental methods

2.1. Materials and synthesis

The synthesis of studtite, $(\text{UO}_2)_2(\text{H}_2\text{O})_2 \cdot 2\text{H}_2\text{O}$, from an initial feedstock of $\text{UO}_2(\text{NO}_3)_2 \cdot 6\text{H}_2\text{O}$ (International Bio-Analytical Industries, Inc., 99.9%) dissolved in a 1% HNO_3 solution to generate a 1.0 M uranyl nitrate solution was detailed previously [8,23]. A significant molar excess of H_2O_2 (30% v/v) was added rapidly to uranyl nitrate hexahydrate solution at room temperature. This resulted in a 5.9:1.0 M ratio of H_2O_2 to $\text{UO}_2(\text{NO}_3)_2 \cdot 6\text{H}_2\text{O}$. The initial pH of the solution was 1. The precipitation of studtite was allowed to occur for 30 min at room temperature. The resulting studtite in solution was not drained or washed of the residual nitrates, before being transferred into an oven at 80 °C for 24 h of drying. The resulting material was lightly ground in an aluminum oxide mortar and pestle, and p-XRD indicated that the material consisted of a mixture of uranyl nitrate trihydrate, metastudtite, and diuranyl dihydroxide bis(nitrate) tetrahydrate. Utilizing the calcination procedures detailed previously, the unwashed material was calcined at temperatures of 350, 400, 450, 500, and 550 °C [8,23]. The calcination products were stored at room temperature in a vacuum chamber at 20 kPa.

2.2. Powder X-ray diffraction (p-XRD) analysis

Powder XRD patterns of the starting material and the various

calcination products were acquired at room temperature on a Bruker D2 PHASER diffractometer with a 1-D LynxEye detector using $\text{Cu K}\alpha$ X-rays ($\lambda = 1.5418 \text{ \AA}$) operating at 30 kV and 10 mA. The instrument was calibrated with a CeO_2 NIST SRM 674b standard using structural data for CeO_2 refinement from Kümmerle et al. [24]. A divergence slit of 0.6 mm, an anti-scattering beam knife height of 1 mm, and a 3 mm receiving slit were used for the sample data acquisition. The quantitative analysis patterns were collected in the Bragg-Brentano geometry (Coupled $2\theta/\theta$) with a scan range of 10–90° 2θ , step size increments of 0.02° 2θ , and 2.5 s per step.

Two methods of performing quantitative analysis of the amorphous phase content were selected: the internal standard method with Rietveld refinement, and the degree of crystallinity (DOC) method as implemented in the X'Pert Highscore Plus v2.2d software [25]. For quantitative analysis sample preparation, samples of ca. 200 mg were wet ground in a high-purity Zirconia mortar and pestle with 2 mL of n-pentane (99+%, extra pure, anhydrous, Acros Organics). Following grinding and room temperature drying, the powder samples were sieved to < 20 μm with an ASTM E11 certified No. 635 test sieve. For the internal standard method, the sieved samples were spiked with 20 wt% Cr_2O_3 (NIST SRM 674b), and well mixed in a 5 mL vial on a vortex mixer. Samples of ca. 50 mg were front-loaded on a P-type B-doped silicon crystal zero diffraction plate. The sample holder was rotated at 24 rpm during the scans to reduce the impact of preferred orientation and improve the counting statistics for the acquired patterns. For the quantification routine, a background was manually fit due to the difficulty in fitting the patterns with high amorphous content. The refined parameters for all phases were the scale factors, specimen displacement, lattice parameters, peak shape parameters, overall isotropic displacement parameters, and preferred orientation. The peak shapes were modeled using a pseudo-Voigt function. Starting models for the structural refinements for α - UO_3 (PDF#01-072-0246), α - U_3O_8 (PDF#01-073-6293), Cr_2O_3 (PDF#01-070-3766), α - $\text{UO}_2(\text{OH})_2$ (PDF#01-074-4842), $(\text{UO}_2)_4\text{O}(\text{OH})_6(\text{H}_2\text{O})_5$ (PDF#01-070-4765), $\text{UO}_2(\text{NO}_3)_2(\text{H}_2\text{O})_3$ (PDF#01-073-4459), $(\text{UO}_2)_2(\text{OH})_2(\text{NO}_3)_2(\text{H}_2\text{O})_4$ (PDF#01-070-0176), $((\text{UO}_2)_2(\text{H}_2\text{O})_2)(\text{NO}_3)_2(\text{H}_2\text{O})$ (PDF#01-072-3827), and $(\text{UO}_2)(\text{NO}_3)_2(\text{H}_2\text{O})_2$ (PDF#01-072-2333) were acquired from the ICDD PDF-2 2008 database [26]. Additionally the starting structural model for $(\text{UO}_2)_2\text{O}_2(\text{H}_2\text{O})_2$ was taken from Weck et al. [27].

2.3. Differential scanning calorimetry

Differential scanning calorimetry (DSC) was performed using a Netzsch DSC 3500 Sirius. Calibration of the temperature and detector sensitivity was performed at a heating rate of 10 °C/min using the onset temperature of melting and heat curve peak areas for Adamantane, Indium, Tin, Bismuth, and Cesium Chloride. The details of the sample preparation and acquisition parameters were presented previously [8].

2.4. Thermogravimetric analysis–mass spectrometry (TGA-MS)

Thermogravimetric analysis combined with online mass spectrometry (TGA-MS) was performed using a TA Instruments SDT Q600 coupled with a Pfeiffer ThermoStar GSD 320 T3 that contains a PrismaPlus mass spectrometer. The mass spectrometer was operated in the selected ion mode for the following ions: $m/z = 14$ (N^+), 16 (O^+), 17 (OH^+), 18 (H_2O^+), 30 (NO^+), 32 (O_2^+), 44 (N_2O^+), and 46 (NO_2^+). Sample preparation and data acquisition details were presented previously [8]. The TGA was calibrated for temperature using the melting point onset temperatures for indium (m.p. = 156.60 °C), zinc (m.p. = 419.53 °C), aluminum (m.p. = 660.32 °C), and silver (m.p. = 961.78 °C).

2.5. UV–Vis

In order to approximate the water-soluble nitrate concentration in

the unwashed uranyl peroxide samples, UV–vis spectroscopy was performed on a Cary 300 spectrophotometer with 1-cm path length quartz cuvettes. A calibration curve was generated using $\text{UO}_2(\text{NO}_3)_2 \cdot 6\text{H}_2\text{O}$ (International Bio-Analytical Industries, Inc., 99.9%) dissolved in DI water (18.2 M Ω) and diluted to concentrations of 1, 4, 6, 8, and 10 ppm NO_3^- . A 50.2 mg sample of dry unwashed uranyl peroxide sample was added to 50 mL of DI water and the water-soluble nitrates were allowed to dissolve for 4 h at 23 °C with periodic agitation prior to dilution to the desired concentration. The transfer of the calibration and investigated sample solutions was performed with glass pipettes packed with glass wool to filter out any undissolved solids. Spectra were acquired over the range of 190–450 nm, with an interval of 0.5 nm, and a scan rate of 300 nm/min. Baseline correction was performed using DI water in quartz cuvettes. Peak absorbance for NO_3^- was 199.5 nm, within the range reported in literature [28] (see Figs. A.1 and A.2).

2.6. Scanning electron microscopy (SEM)

The initial metastudtite/uranyl nitrate samples and the 15 α - UO_3 calcination product samples were prepared for SEM by dusting 5–10 mg of each sample on top of a 12 mm conductive carbon tab that was adhered to a 12.7 mm aluminum pin stub mount. The initial metastudtite/uranyl nitrate samples and the 350 °C calcination products required coating with 20.2 ± 0.1 nm of Au/Pd film due to excessive surface charging. Images of the samples were collected on a FEI Quanta 600 FEG scanning electron microscope. The acquisition parameters were detailed previously [8]. Within each sample, 3–4 macro-particles were selected for detailed high-magnification examination. At least 10 secondary electron images were acquired on each macro-particle surface at magnifications ranging from 5000 to 30,000 \times . Over one thousand secondary electron images were acquired for further morphological analysis. Particles from the SEM images were segmented using the MAMA software as previously described [8].

2.7. Machine learning analysis

In addition to the manual particle segmentation, machine learning was performed using convolutional neural networks to classify α - UO_3 images according to their respective calcination temperatures. Lecun et al. first demonstrated the capacity of multilayer neural networks trained with the backpropagation algorithm to classify high-dimensional patterns [29]. The backpropagation algorithm makes use of a gradient descent to iteratively update a network's weight values, calculating the gradient of a pre-determined loss function with respect to the weights in each step. It propagates backwards in the sense that the gradient is calculated for the network's layers in reverse order, beginning from its final layer. The training process uses the disparities between the known labels of input training data and the network's outputs to evaluate the loss function. Once appropriately trained, a multilayer neural network can recognize patterns among features that may not be immediately identifiable to humans. While the descriptions of these features may prove difficult to later reconstruct from an analysis of the networks' operation, they can already provide for image classification via statistical comparison of the similarities found among the images in different databases. Performing this kind of experimentation requires only a Visual Geometry Group (VGG) model such as that proposed by Simonyan and Zisserman [30].

The architecture of the network (VGG-16) that was utilized for these experiments consists of sixteen layers. The VGG model contains thirteen convolutional layers (i.e., layers that apply the inner product of a square weight mask to image neighborhoods prior to passing the results to the succeeding layers) with rectified linear unit (ReLU) activations (i.e., activations of the form $\text{ReLU}(x) = \max(x, 0)$). Convolutional layers without a nonlinear activation are linear filters. A cascade of multiple convolutional layers without nonlinear functions is still a linear filter; therefore, ReLU activations follow each convolutional layer

to allow the network to learn highly non-linear functions. In the VGG model, convolutional layers are followed intermittently by max pooling (i.e., a pruning process in which each square image neighborhood of a fixed size is collapsed to a single pixel having an intensity value equal to the maximum intensity value found in the original image neighborhood). The role of max pooling is to reduce the spatial size of the intermediate feature representations and to build translation invariance into the network. The VGG model also incorporates three fully-connected layers after the convolutional layers (i.e., layers with connections from every neuron to every neuron in the preceding layer, also with ReLU activations), and finally followed by a softmax (i.e., a procedure that, by normalizing the exponentials of each value in a given vector, converts that vector into a discrete probability distribution). The role of fully-connected layers is to learn the classification function using the output of the final convolutional layer as a feature space. The softmax function normalizes the outputs of the network such that they can be interpreted as class probabilities. A diagrammatic description of the VGG-16 network that was utilized for these experiments, drawn to scale according to the sizes of each of the layers, appears in Supplemental information Fig. A.3. Please refer to this diagram for more information regarding the precise features of the neural network. Having already been trained to correctly classify a variety of everyday images including images of various types of animals, vehicles, and household objects, the model comes equipped with a set of pre-determined weight values [31].

Using the VGG-16 network, four binary classifications were performed. Images at the calcination temperature of 350 °C were classified against those at each of the other calcination temperatures (i.e. 400 °C, 450 °C, 500 °C, and 550 °C). For consistency, only images acquired at 15,000 \times magnification and with a resolution of 2048 \times 1887 pixels were used. All images were pre-processed in MathWork's MATLAB Version R2017a and Apple's Preview Version 10.0 [32]. Pre-processing consisted of making the images monochromatic, removing their data labels, equalizing their pixel intensity value histograms (if necessary), and breaking each into four separate, non-overlapping images of size 1024 \times 863 pixels. Additionally, the images of size 1024 \times 863 were converted from the .tif to the .jpeg format. This resulted in 468 images at 350 °C, 364 images at 400 °C, 128 images at 450 °C, 140 images at 500 °C, and 36 images at 550 °C. Ten images were randomly selected from each temperature group and set aside for the purposes of testing the four resultant classifiers. These images were not used when training the four neural networks.

3. Results and discussion

3.1. Thermal decomposition analysis

Investigating the chemical transitions that occur as a starting material decomposes is critical to understanding the consequent changes in the material's morphology. The acts of dehydration, denitration, and reduction all likely play a role in the calcined product's morphology. To that end, DSC, TGA-MS, and p-XRD were utilized to monitor the thermal decomposition of an unwashed uranyl peroxide precursor.

The dried samples of unwashed uranyl peroxide appeared, to the naked eye, to have a glassy/crystalline texture and were dark yellow in color. In the bottom of the platinum crucible used for calcination, the material had the appearance of almost being melted to the bottom of the vessel. It required grinding to break up the sample prior to analysis. In contrast, previously synthesized samples of washed uranyl peroxide resulted in a light yellow powder with a granular texture [8]. The unwashed uranyl peroxide starting material, through p-XRD analysis, was found to consist of a mixture of $73.2 \pm 2.1\%$ $(\text{UO}_2)(\text{NO}_3)_2(\text{H}_2\text{O})_3$, $13.5 \pm 2.2\%$ $(\text{UO}_2)\text{O}_2(\text{H}_2\text{O})_2$, and $13.3 \pm 2.1\%$ of the dimer $[(\text{UO}_2)_2(\text{OH})_2(\text{NO}_3)_2(\text{H}_2\text{O})_3] \cdot \text{H}_2\text{O}$ (Fig. 1). These results suggest that although uranyl peroxide was formed with the addition of hydrogen peroxide, the generated excess nitric acid in solution and the resulting

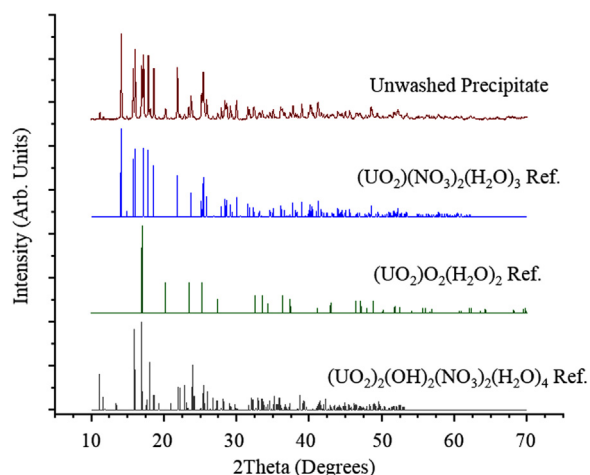


Fig. 1. Powder X-ray diffraction patterns for the initial unwashed uranyl peroxide precipitate compared against the reference patterns for $(\text{UO}_2)(\text{NO}_3)_2(\text{H}_2\text{O})_3$ from PDF #01-073-4459, $(\text{UO}_2)\text{O}_2(\text{H}_2\text{O})_2$ from PDF #00-016-0207, and $(\text{UO}_2)_2(\text{OH})_2(\text{NO}_3)_2(\text{H}_2\text{O})_4$ from PDF #01-070-0176. Rietveld refinement of three samples indicates that the unwashed precipitate consists of $73.2 \pm 2.1\%$ $(\text{UO}_2)(\text{NO}_3)_2(\text{H}_2\text{O})_3$, $13.5 \pm 2.2\%$ $(\text{UO}_2)\text{O}_2(\text{H}_2\text{O})_2$, and $13.3 \pm 2.1\%$ $(\text{UO}_2)_2(\text{OH})_2(\text{NO}_3)_2(\text{H}_2\text{O})_4$. Additional refinement details can be found in Table A.17.

decrease in pH, shifted the chemical equilibrium towards the uranyl nitrate species as noted by Sanderson et al. [33]. The UV–Vis analysis of the unwashed uranyl peroxide indicated 21.5 wt% NO_3^- (Figs. A.1 and A.2), which is in close agreement with the 22.4 ± 0.9 wt% NO_3^- indicated from the p-XRD results.

The unreacted uranyl nitrate hexahydrate dehydrated to the uranyl nitrate trihydrate upon heating and subsequent storage under vacuum. Several researchers have identified the propensity for uranyl nitrate hexahydrate to dehydrate to uranyl nitrate trihydrate in a temperature range of 60–80 °C [34–36], under a flow of dry inert gas [37], or in vacuo [36]. All of those conditions were experienced by the unwashed samples in this study prior to calcination and analysis.

The hydrolysis of a portion of the UO_2^{2+} in solution resulted in the formation of a polynuclear uranyl complex, an aquonitrato complex of the dimer, $[(\text{UO}_2)_2(\text{OH})_2(\text{NO}_3)_2(\text{H}_2\text{O})_3] \cdot \text{H}_2\text{O}$. In solution, the dimer complex, $(\text{UO}_2)_2(\text{OH})_2^{2+}$, is the principal hydrolysis species over a wide range of pH (2–5) and metal concentrations ($> 10^{-4}$ M) [38,39]. Woodhead et al. identified the presence of $[(\text{UO}_2)_2(\text{OH})_2(\text{NO}_3)_2(\text{H}_2\text{O})_3] \cdot \text{H}_2\text{O}$ as a result of a disproportionation reaction in uranyl nitrate hexahydrate due to the loss of water upon heating to 70–80 °C [40]. Several researchers have also noted that the production of polynuclear aquonitrato complexes can occur from the dehydration of uranyl nitrate solutions when the $\text{NO}_3:\text{UO}_2^{2+}$ ratio in solution is between 1 and 1.5 [41–43]. The addition of hydrogen peroxide to the uranyl nitrate solution results in the formation of solid $[(\text{UO}_2)_2(\text{O}_2)(\text{H}_2\text{O})_2](\text{H}_2\text{O})_2$. As the uranyl ion continues to precipitate out of solution, the $\text{NO}_3:\text{UO}_2^{2+}$ ratio in solution will increase, and could explain the formation of the small amount of the dimer complex seen in this study.

The thermal decomposition of uranyl nitrate hydrates has been investigated previously, and is known to occur through a complex set of intermediates [34,35,44–48]. Several studies indicate that the decomposition of uranyl nitrate hydrates does not result in an anhydrous uranyl nitrate intermediate, but rather a hydroxynitrate species [35,44–47]. TGA-MS and DSC were utilized to monitor the decomposition of the multi-component starting material over the temperature range of 25–600 °C (Fig. 2). Samples of nitrate-free metastudite synthesized under similar conditions, were investigated previously using the same TGA-MS methodology [8].

The first endothermic transition identified from the thermal

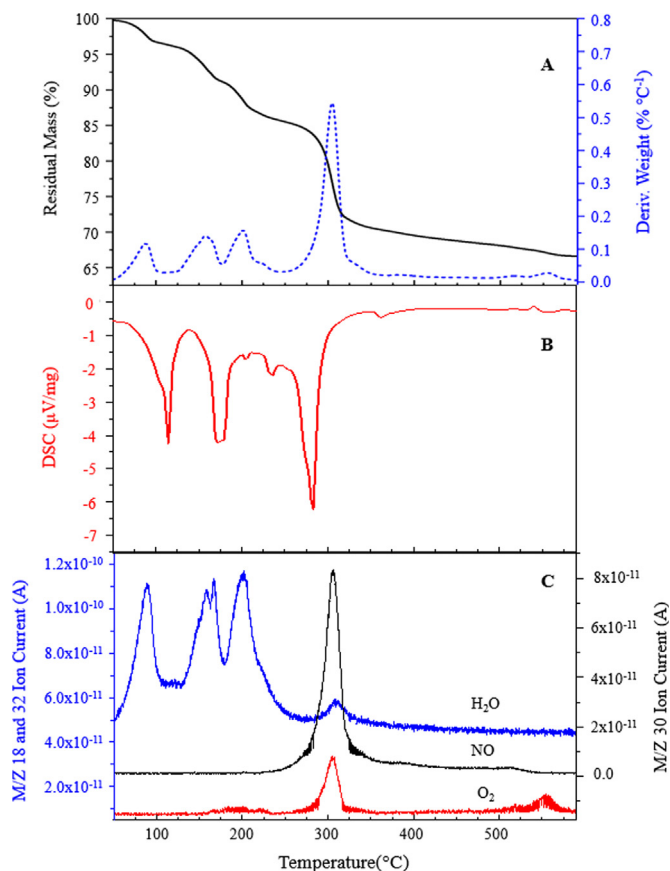


Fig. 2. A) TGA mass loss for the multi-component starting material, and the associated derivative of the mass loss. B) DSC thermogram with exothermic transitions occurring in the upward direction, three replicates were performed with similar results. C) Mass spectrometer readings for H_2O , O_2 , and NO as the starting sample was heated from 25 °C to 600 °C at 10 °C/min with 100 mL/min He flow. A complex series of dehydration events occur up to 250 °C, including the conversion of $(\text{UO}_2)\text{O}_2 \cdot 2\text{H}_2\text{O}$ to am- UO_x ($3 \leq x \leq 3.5$). Nitrate decomposition occurs at 300 °C with the associated conversion to UO_3 . At 550 °C, the conversion to U_3O_8 is registered with the associated increase in MS O_2 signal.

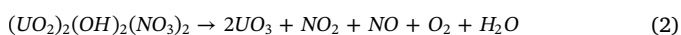
decomposition of the starting material, occurred from 50 to 110 °C and correlated with the loss of one water from the uranyl nitrate trihydrate and one water from the diuranyl dihydroxide bis(nitrate) tetrahydrate to form uranyl nitrate dihydrate and diuranyl dihydroxide bis(nitrate) trihydrate, respectively. Utilizing the p-XRD determined initial masses for each species, the theoretical mass loss for this transition is 3.25%, and the actual TGA mass loss was $3.25 \pm 0.20\%$ (3σ error). The mass spectrometer detected a significant increase in H_2O vapor in conjunction with this mass loss. Previously, Dash et al. [35], Smith et al. [34], and Bridge et al. [36] also observed conversion of the uranyl nitrate trihydrate to the dihydrate in the same temperature range.

The second endothermic transition occurs from 110 to 175 °C, and appears to consist of at least two separate dehydration events occurring in close proximity in temperature. The mass spectrometer signal shows two separate H_2O peaks, and the DSC endotherm is broadened. One of the dehydration events is due to the loss of 1.5 waters from the uranyl nitrate dihydrate, as documented by Dash et al. [35]. The other dehydration event would appear to correlate with the loss of 2.5 waters from the diuranyl dihydroxide bis(nitrate) trihydrate. The total theoretical mass loss for these transitions being 5.19%, with an actual transition mass loss of $5.19 \pm 0.07\%$. Previously, little to no mass loss was recorded up to this temperature for nitrate-free $(\text{UO}_2)\text{O}_2 \cdot 2\text{H}_2\text{O}$ [8]. From 175 to 250 °C, the $(\text{UO}_2)\text{O}_2 \cdot 2\text{H}_2\text{O}$ loses two hydrates and converts to an x-ray amorphous UO_x ($3 \leq x \leq 3.5$) as has been documented previously for the thermal decomposition of washed uranyl peroxide hydrates

[8,49–52].

To assess intermediates formed from the uranyl nitrate hydrates, a sample of unwashed uranyl peroxide was calcined for 8 h in air at 200 °C, cooled to room temperature, and subsequently analyzed by p-XRD. No $\text{UO}_2(\text{O}_2)\cdot 2\text{H}_2\text{O}$ was detected, having been converted to x-ray amorphous material (Fig. A.4). An additional DSC endotherm occurs at 225 °C with a slight increase in the H_2O signal on the mass spectrum.

The third endothermic transition is the largest, resulting from nitrate decomposition at 250 °C (see Fig. 2B). The mass spectrum shows significant signals for NO (m/z 30) and NO_2 (m/z 46) at 306 °C (Fig. 2C). Significant H_2O and O_2 signals also correlate with the decomposition of the uranyl nitrate hydrate and the dimer complex according to the reactions:



Interestingly, the nitric oxide mass spectrometer signal does not return to baseline until 525 °C. This second stage release of nitric oxide out to 525 °C was also seen by Dash et al. during the thermal decomposition of uranyl nitrate hexahydrate at the same heating rate of 10 °C/min and was attributed to product barrier layer formation delaying the release of entrained nitrates [35]. The theoretical total mass loss for the conversion of all the initial species to UO_3 is 31.91%, and the actual TGA mass loss by 360 °C was $29.28 \pm 0.47\%$. The 2.6% mass loss discrepancy can be accounted for by the residual nitrates and/or the slow conversion of am- U_2O_7 to am- UO_3 as was previously observed in the decomposition of metastudtite [8,49].

An endotherm is registered on the DSC at 360 °C, but without an associated increase in NO_x or O_2 and no step change in mass. This endotherm was seen by Kalekar et al. at a temperature of ca. 370 °C and was associated with the release of additional nitrates, and could also be associated with the transition from am- UO_3 to α - UO_3 as seen in the qualitative p-XRD results (Fig. 3). The only exothermic transition registered during the course of the thermal decomposition is at 540 °C. It coincides with the release of O_2 and a mass loss corresponding with the generation of U_3O_8 as seen on the p-XRD of a sample calcined at 550 °C (Fig. 3). The total theoretical mass loss for the conversion of the starting material to U_3O_8 is 33.27%, and the actual mass loss by 590 °C was $33.08 \pm 0.44\%$.

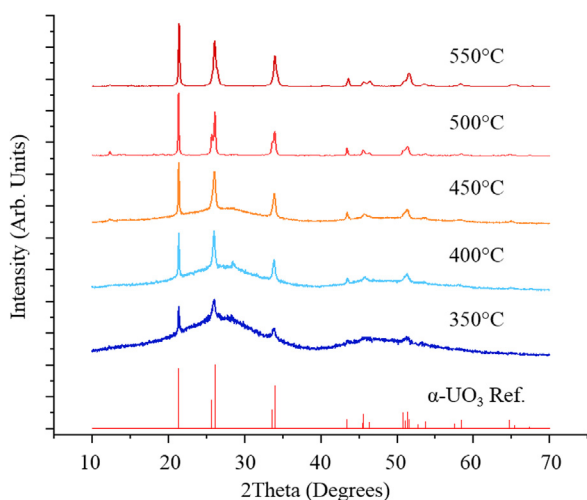


Fig. 3. Qualitative powder X-ray diffraction patterns for the calcination products from unwashed uranyl peroxide precipitate held at the indicated temperatures for 8 h in air. The reference pattern for α - UO_3 from PDF#01-072-0246 is included for comparison. As the calcination temperature increases, the amorphous content decreases with a commensurate increase in α - UO_3 crystalline phase. By 550 °C, the presence of a small amount of α - U_3O_8 is also detected.

3.2. Qualitative morphology analysis

The initial unwashed uranyl peroxide was investigated under the SEM, and compared to previously synthesized washed uranyl peroxide [8] (Fig. 4). It is evident that the resulting materials are distinctly different. The unwashed material exhibits acicular features; while the washed material exhibits sub-rounded grains. The precipitation of uranyl peroxide, and the resulting morphology, is heavily influenced by the concentration of the involved species, the ionic strength, temperature, and the pH [22,33,53]. As Cordfunke previously noted, needle like crystals can be formed during the precipitation of uranyl peroxide solutions in the presence of high nitric acid due to the resulting slow formation of complexes of uranyl and peroxide ions [45]. The uranyl nitrate solution in this study contained a high concentration of nitric acid. The presence of a mixture of uranyl nitrate trihydrate and uranyl peroxide in the dehydrated product indicates that the competition between the peroxide and nitrate ions likely slowed the formation of uranyl peroxide; therefore, resulting in needle-like features.

The resulting products from the calcination at temperatures of 350, 400, 450, 500, and 550 °C were also investigated thoroughly under the SEM. Representative images of the resulting surface features can be seen in Fig. 5. The morphological differences appear very drastic between the calcination temperatures. Tamasi et al. previously developed a lexicon of descriptors for describing nuclear material images for the purpose of nuclear forensics [54,55], and these descriptors were applied to the calcination products in this study.

The macro-particles (ca. 50–500 μm in size) in the initial unwashed material were a *complex conglomerate*, consisting of micro-particles (< 1 μm in size) that exhibited a wide variance in morphology. The overall morphology of the macroparticle was *rounded* or *blocky*, with the macro-particle edges having morphologies that ranged from *sub-rounded* to *very angular* and of an *irregular medium sphericity*. The angular nature of the edges is attributed to the fact that the bulk material initially consisted of a melt that was fragmented prior to calcination or microscopic investigation. Several of the investigated macro-particles were seen to have *conchoidal fracture features*, curved breakages similar to that seen in fragmented obsidian, present on the surface. These fracture features and *vitreous* character of the morphology are also indicative of the fragmentation from the melt that occurred during the low-temperature dehydration. There are portions of the macro-particle surface that appear *porous* and there is also some slight *dendritic* fracturing of a shallow depth. These macro particle features remained relatively consistent across all temperatures with only slight variations. For example, spherical bubbles and large pore cavities that penetrate deep into the macro particles formed on the 350 °C samples (Fig. 6A). These are likely a result of the decomposition products. Furthermore, at 500 and 550 °C, the sintered micro particles created features that were clearly visible on the macro particle surface (Figs. A.5–A.7).

The micro-particles that compose the bulk of the unwashed uranyl peroxide starting material, are of an *acicular*, or needle-like, nature. These acicular particles are *straight* and, qualitatively, appear to have an average aspect ratio of ca. 4:1. There exists another much smaller population of particles on the surface that are *sub-rounded* grains. The spatial grouping of the acicular features is generally *irregular* with no coherent ordering to their orientation. In rare instances, *radiating rosettes* of acicular features were found (see Figs. A.5–A.12 for additional examples of the discussed morphology).

At the micro-particle level, the 350 °C sample shows three distinct developments from the starting material: the formation of surface *pores*, large *channels/cavities*, and *parallel rhomboidal* surface grains. The boundary of the surface pore edge can vary from being irregular to rounded. Furthermore, the surface pores seem to occur heavily in isolated regions over a 25 μm^2 region of the surface, and the regions can be separated by as much as 5–10 μm . When the rhomboidal surface grain morphology occurs, it is co-located within these surface pore regions. The rhomboidal grains seem to generally orient themselves in a parallel

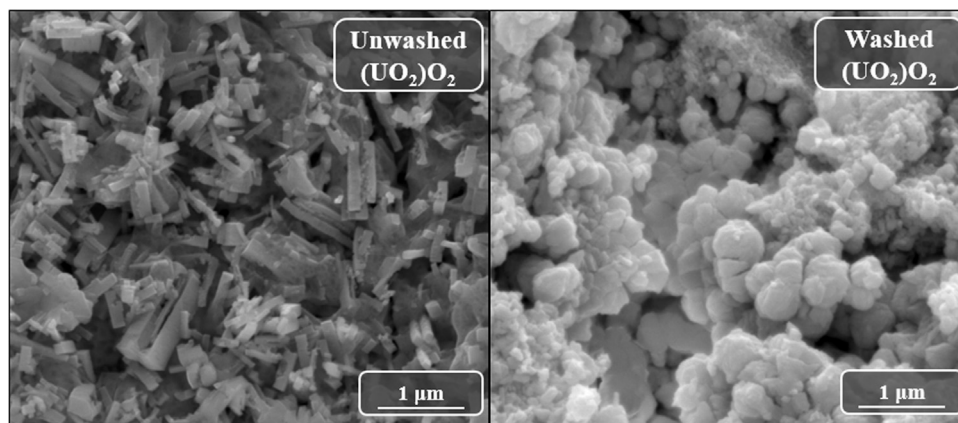


Fig. 4. Comparison of unwashed (left) and washed (right) uranyl peroxide precursors from hydrogen peroxide precipitation in uranyl nitrate solution showing distinct differences in morphology.

direction on the surface of the particle across the localized region where they occur.

In general, as the calcination temperature is increased, the density of surface pores increases. At 400 °C, 450 °C, and 500 °C, the surface pores form a complex *reticulated*, or net-like, pattern that spreads across the majority of the macro-particle surface (Fig. 6B). The rhomboidal grain density increases to the point that there is considerable overlap between grains, and the grains in a localized region are still generally oriented in one direction. By 400 °C, the surface grains begin to appear porous themselves, and become very rough rather than smooth and faceted.

The 450 °C samples had a significantly lower surface grain and surface pore density than either the 400 °C or 500 °C samples. The 500 °C sample shows the most dramatic transformation, with almost complete coverage of the surface with the rhomboidal surface grains.

The reticulated network of surface pores is visible underneath the surface grains. A third population of even smaller surface nanopores (10–50 nm) begin to form across the entire surface at 500 °C, including on the surface grains and acicular features themselves (Fig. 6C). As was noted from the TGA-MS data, the slow release of NO_x from 300 °C to 525 °C is likely due to the formation of a dense product layer barrier. Yu et al. previously identified during calcium oxide synthesis that an outer product layer can trap gaseous decomposition products, resulting in internal pressures that cause the formation of both smaller surface pores and larger channels on the surface of the material [56].

By 550 °C, significant sintering has occurred. The rhomboidal surface grains are almost completely sintered, with the surface of the particle losing almost all definition. The reticulated surface pore network also appears predominantly sintered, and those pores that do remain appear to be very shallow and rounded. The surface nanopores

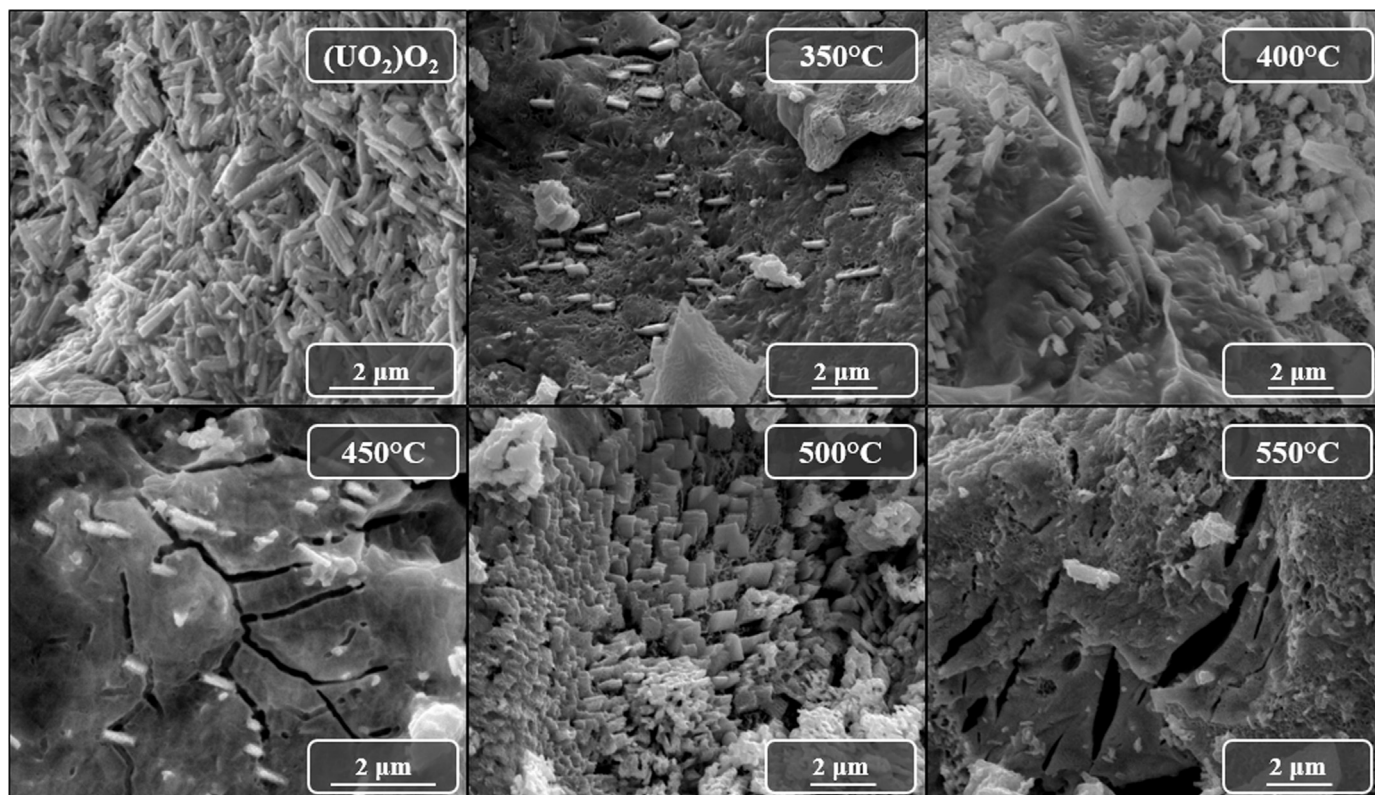


Fig. 5. Representative SEM Images of the unwashed $(\text{UO}_2)_2\text{O}_2$ starting material and the calcination products as a result of heating the sample at 350, 400, 450, 500, and 550 °C in air for 8 h.

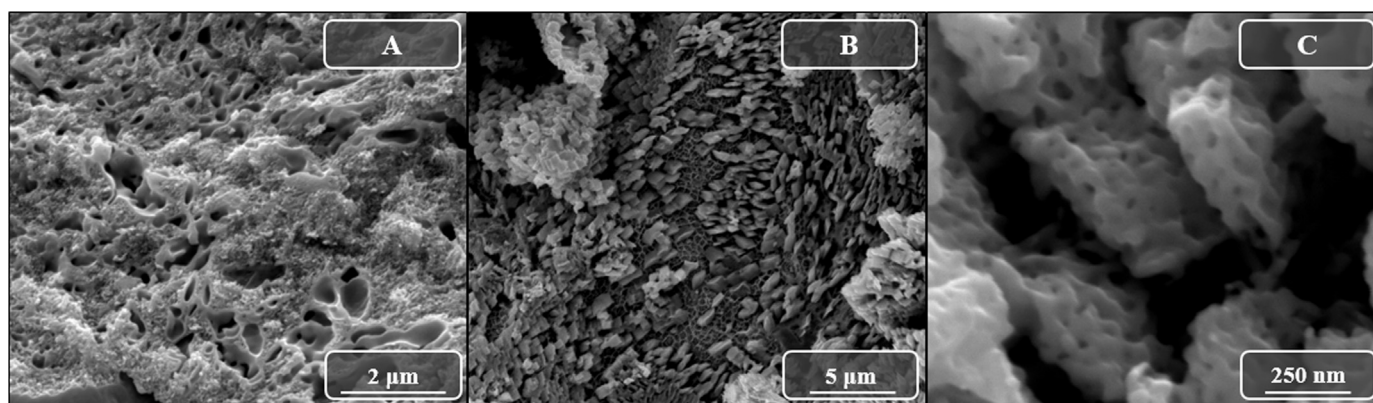


Fig. 6. A) Image of 350 °C calcination product surface highlighting the large pores and channels that form on the surface of calcined unwashed uranyl peroxide. B) Image of 500 °C calcination product surface highlighting the surface grain extent and the reticulated network of surface pores that are visible underneath the surface grains. C) Image of 500 °C calcination product surface showing a sampling of the surface nanopores that form at 500–550 °C.

that were ubiquitous at 500 °C, also occur across the particle surface at 550 °C. The 550 °C samples appear to have a higher density than the lower temperature samples, from the apparent loss of void spaces. The surface cavity population density decreased as some of the fissures seem to sinter back together.

From the qualitative analysis, several discerning characteristics that can act as forensic signatures have been identified. It is important to note that the most distinct features came from the micro particles. It can be seen that the initial starting material contains no rhomboidal surface grains or surface pores. The 350 °C samples show very limited surface grain and surface pore formation. The 400–450 °C samples show significant surface grain and pore formation, but do not have the surface nanopores forming on the surface. The 500 °C samples show extensive surface grain and surface pore formation, and the surface nanopores first make their appearance at this temperature. The 550 °C samples exhibit significant sintering, a loss of the majority of the surface grains and reticulated pores, but retain the presence of the surface nanopores. These distinct features were further probed using particle segmentation to try to identify statistical differences between the different calcination temperatures.

3.3. Quantitative morphology analysis

Quantitative analysis was performed on the starting material and all calcination temperatures. In total, fourteen attributes ranging from vector area to ellipse perimeter were calculated for each segmented particle (Tables A.1–A.16). Three main features seen throughout the calcination of the unwashed uranyl peroxide were chosen for statistical analysis: the long acicular needles, rhomboidal surface grains, and surface pores. An additional signature, large cavities that penetrate into the surface with an indeterminate depth, were initially investigated for segmentation, but due to a limited population across all temperatures were not pursued further. The acicular needles were considered the most promising signature, due to their presence at every investigated calcination temperature, as well as being the only signature present in the unwashed starting material. In accordance with segmentation inclusion guidelines discussed previously [23], only features that had defined edges and were unobstructed were considered viable for quantitative analysis. For the segmentation of the surface pores, only pores with defined edges that were shallow enough to allow visibility to the bottom of the pore were included for segmentation. An example of the manual segmentation can be seen in Fig. 7.

In this study, a minimum of 500 segmented particles for each feature type, at each temperature, was investigated. This value is based on the maximum particles that could be segmented in the microscopy images. As multiple features were present within any given image, the surface density of that given feature was low; thus limiting the segments

of each feature. Nonetheless, the combination of all three features resulted in over 1500 segments for each calcination temperature.

The results of the quantitative morphological analysis for the long, acicular needle features can be seen in Fig. 8. The long needles appear to increase in their equivalent circular diameter (ECD) from the initial unwashed uranyl peroxide up to a calcination temperature of 400 °C [57]. The needle features then begin to decrease in size above 400 °C as a result of sintering that was previously seen to occur in the range of 400–450 °C for washed uranyl peroxide [8]. Extensive sintering occurs by 550 °C, and the longer needles appear more likely to be obstructed by, or embedded in the sintered surface, resulting in a decrease in quantified size. The ellipse aspect ratio of the acicular needles shows only slight variations as a function of temperature, with an average aspect ratio of ca. 3.

The results of the rhomboidal surface grain segmentation can be seen in Fig. 9. The ECD results do not show a consistent trend as a function of increasing temperature. The 350, 450, and 550 °C samples were those which had the lower surface grain density across their respective surfaces. The 400 °C and 500 °C samples had extensive surface grain growth. One observation when comparing the morphology seen in these two separate groups (See Figs. A.6 and A.11), is that there appears to be an impact in the quantified size due to the orientation of these surface grains. The surface grains in the acquired images for the 350, 450, and 550 °C samples are oriented in such a way that they appear more rectangular, while the 400 °C and 500 °C samples clearly show a more rhomboidal shape. It is unknown what would cause this variation in surface grain orientation as a function of temperature. The circularity of the samples exhibits a minimum at the sintering temperature of 400–450 °C, and subsequently increases with temperature.

The results of the shallow surface pore segmentation can be seen in Fig. 10. The ECD of the surface pores shows little variation between the 350, 400, and 500 °C samples. Reticulated networks were not as dominant in the 350, 450 °C, and 550 °C samples which may explain the significant deviation from the neighboring distributions. The 550 °C samples experienced sintering that reduced the size of the surface pores and also had a population of nanopores that drove the ECD much lower at this temperature. In general, the surface pore circularity increased as a function of calcination temperature. It is evident from the confidence intervals displayed on the quantitative morphology results, that no single feature attribute was sufficient to differentiate all calcination temperatures. Therefore, additional signatures were sought to improve the ability to discriminate these samples as a function of calcination temperature.

3.4. Quantitative p-XRD analysis

Qualitative XRD analysis demonstrated differences between each of

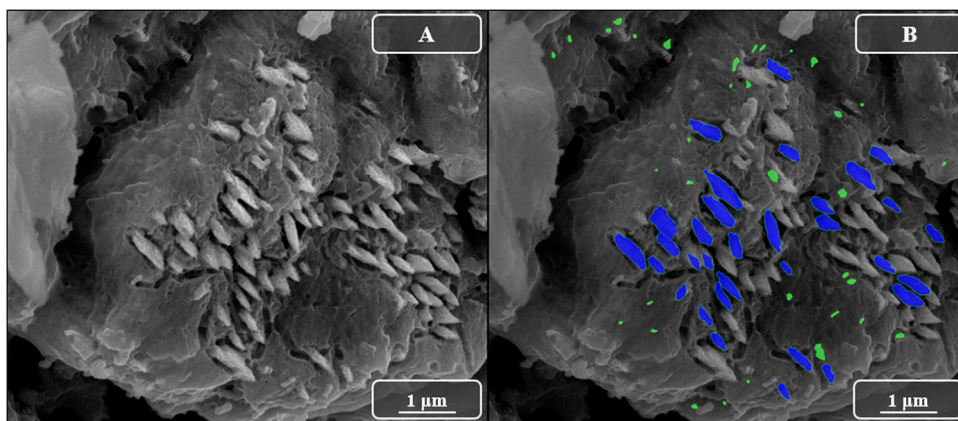


Fig. 7. Images A and B show the electron microscopy image before and after segmentation of the surface grains (blue) and pores (green) for a sample from 450 °C. Only surface pores and grains in which all edges were clearly visible were segmented for statistical analysis.

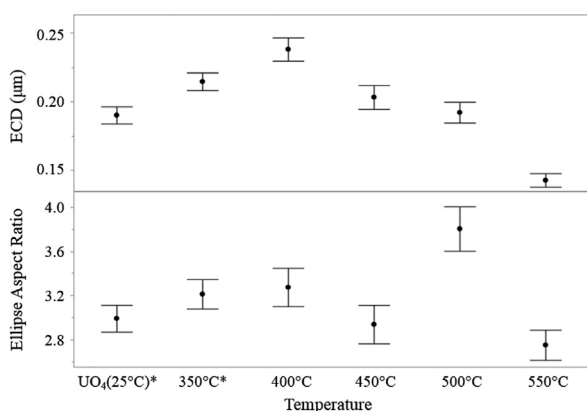


Fig. 8. Top) Equivalent circular diameter, ECD, for the acicular surface features as a function of temperature from the manually segmented SEM images. Bottom) Ellipse aspect ratio for the acicular surface features as a function of temperature from the manually segmented SEM images. The error bars correspond to the 99% confidence interval for the mean of each group. *The unwashed uranyl peroxide starting material and the 350 °C sample were coated with a thin film of Au/Pd due to surface charging.

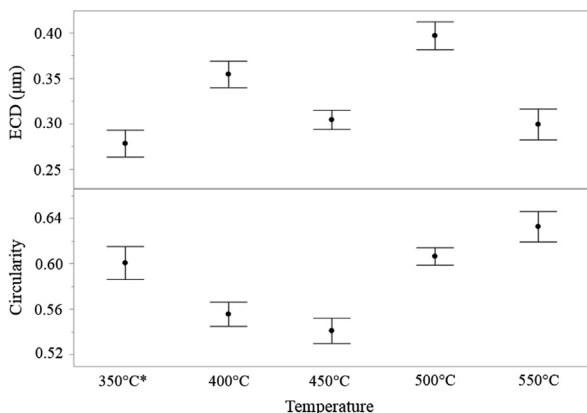


Fig. 9. Top) ECD, for the rhomboidal surface grain features as a function of temperature from the manually segmented SEM images. Bottom) Circularity for the rhomboidal surface grain features as a function of temperature from the manually segmented SEM images. The error bars correspond to the 99% confidence interval for the mean of each group. *The 350 °C sample was coated with a thin film of Au/Pd due to surface charging.

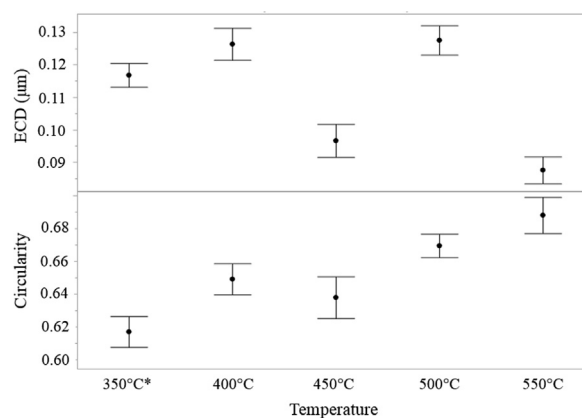


Fig. 10. Top) ECD, for the surface pore features as a function of temperature from the manually segmented SEM images. Bottom) Circularity for the surface pore features as a function of temperature from the manually segmented SEM images. The error bars correspond to the 99% confidence interval for the mean of each group. *The 350 °C sample was coated with a thin film of Au/Pd due to surface charging.

the calcination temperatures (Fig. 3). Hence, the degree of crystallinity and Rietveld Refinement were performed to quantify the crystallographic differences. To our knowledge, this is the first time that the quantitative phase analysis of the amorphous content has been utilized for pre-detonation nuclear forensics. As Jenkins and Snyder noted, amorphous phase quantification is rarely performed due to the time-intensive sample preparation and setup [58].

The background intensity for a scan arises as a result of detector noise, scattering from the sample and air, x-ray fluorescence, and other sources [59]. The measured intensity that is not due to the crystalline phase(s) or the background, is attributed to the x-ray amorphous component of a sample. The DOC method, as implemented, assumes a constant background that has been calibrated against a standard of the same elemental composition and density with a known crystallinity content. The DOC crystallinity % was determined by taking the intensity ratio of the crystalline diffraction peaks, and the total of all measured intensity that has been corrected for the background [25]:

$$Crystallinity [\%] = 100 * \frac{\sum I_{crystalline}}{\sum I_{total} - \sum I_{const. background}} \quad (3)$$

The amorphous content was assumed to be equal to the remainder of the sample that wasn't assigned as crystalline. In this study, a well characterized α -UO₃ standard was not readily available. Therefore, the

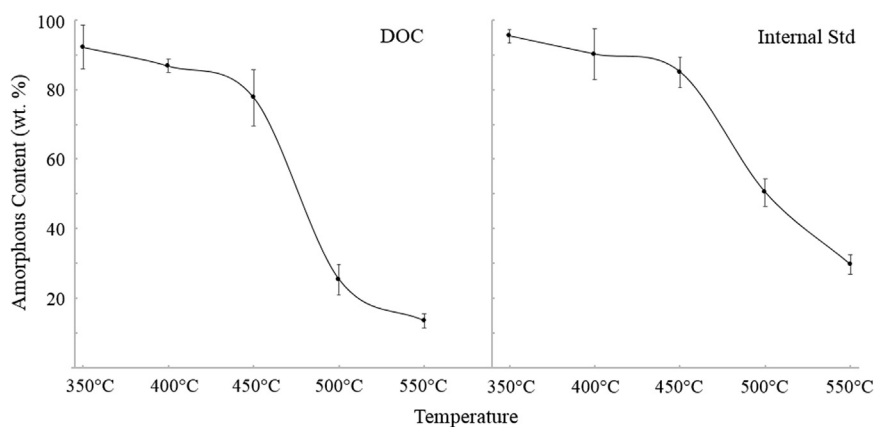


Fig. 11. Mean amorphous content (wt%) as a function of calcination temperature. The degree of crystallinity (DOC) and the internal standard method as indicated. 95% confidence interval of the mean shown.

constant background was determined for each sample by taking the average of the constant background at the low and high angle portion of the most crystalline scans (550 °C). The degree of crystallinity method, while less accurate than many other methods, is useful in instances where structural data is not available for the phases of interest [59,60]. This allows for comparison of the various calcination products within this study, but precludes their use for comparison against externally analyzed samples. The results of the degree of crystallinity analysis can be seen in Fig. 11. It is apparent that the amorphous content decreases as the calcination temperature increases. At the 95% confidence interval, there is significant overlap between the 350 °C and 400 °C temperatures. All other temperatures were found to be significantly different at even the 99% confidence level.

A separate method, the Rietveld method, was also performed as it utilizes the addition of an internal standard and refinement of the full XRD pattern for determination of the phase contents. The Rietveld method is considered one of the most reliable means of acquiring quantitative phase contents, although it does require known atomic structural data for the phases present in the investigated mixture [59,61]. Bish and Howard detail the use of an internal standard with Rietveld refinement to determine the amorphous content [62]. The results of the internal standard quantitative phase analysis can be seen in Fig. 11. Details for the refined patterns at each temperature can be seen in Figs. A.13–A.17, and Tables A.17–A.22. The trend of decreasing amorphous content with increased temperature closely matches that of the DOC. It is apparent that the DOC method overestimates the amorphous content at the higher temperatures. One source of possible error in the internal standard method could be due to microabsorption effects that result from differences in particle size, degree of particle aggregation, and the linear absorption coefficient between the internal standard and the investigated phase [59]. The Brindley microabsorption correction was not applied in this case, due to the product of the linear absorption coefficient (est. $0.188\text{--}0.190\ \mu\text{m}^{-1}$) and particle size (ca. 20 μm) of the $\alpha\text{-UO}_3$ phase falling outside the bounds where the correction is applicable [63,64].

At 350 °C, the $\alpha\text{-UO}_3$ peaks were very weak compared to the amorphous background. The 400 °C sample would rapidly hydrate leading to trace amounts of $\alpha\text{-UO}_2(\text{OH})_2$ that were quantified. In contrast to the SEM analysis, where the samples were only exposed to atmospheric air briefly as they were transferred into the instrument, the three, 400 °C XRD samples were exposed to atmospheric air for increasing lengths of time while waiting for the prior sample to complete XRD analysis (up to 7 h for the last replicate). The first sample registered < 1% of the hydroxide, the second replicate 2.3%, and the last replicate had 1.9% $\alpha\text{-UO}_2(\text{OH})_2$ with 2.0% metaschoepite ($\text{UO}_3\cdot 2\text{H}_2\text{O}$). This rapid hydration is likely due to the presence of am- U_2O_7 in these low temperature samples. Odoh et al. previously showed am- U_2O_7 from

uranyl peroxide to be hygroscopic and water reactive resulting in metaschoepite formation [50].

The 450 °C and 500 °C samples also exhibit weak superlattice reflections that were previously identified by Tsvignov and Kuznetsov when they were investigating the calcination of uranyl nitrate hexahydrate, uranyl peroxide with residual nitrates, and washed uranyl peroxide [65]. The 450 °C samples exhibit only one weak reflection consistent with the $\alpha\text{-UO}_{2.87}$ or $\alpha\text{-UO}_{3.01}$ phase. The 500 °C samples exhibit a series of superlattice reflections consistent with the $\alpha\text{-UO}_{2.87}$ phase. Naito et al. noted that while defect structures, like lattice vacancies and interstitial atoms, are often randomly distributed, there can exist compositions that result in the defects arranging in some order and resulting in the presence of superlattice lines in uranium oxides [66]. The 550 °C samples also begin to show the presence of $\alpha\text{-U}_3\text{O}_8$ which correlates with the TGA mass loss and O_2 release that occurred at this temperature. At the 95% confidence interval, the 400 °C sample cannot be differentiated from the 350 °C or 450 °C samples based on amorphous content. Nonetheless, the 500 °C and 550 °C samples are statistically distinct from each other and all other temperatures.

3.5. Statistical comparison analysis

Although all of the analytical techniques discussed above provided unique features for classification of the various calcination products, the morphological and amorphous content signatures, separately, were insufficient to statistically distinguish all calcination temperatures. The combination of multiple quantitative forensic signatures to provide information on the process history lies at the core of nuclear proliferomics. Therefore, a method of analyzing a combination of multiple quantitative signatures with their associated uncertainties was used to couple multiple morphological signatures crystallinity signatures into a conclusive differentiation of calcination temperature.

Parker previously addressed the issue of using sets of numerical forensic evidence and ascribing the probability a set of samples share the same origin at a specified level of confidence [67–69]. The approach devised by Parker utilizes the number of signatures that may be acquired at a crime scene, and after taking into account the measurement and sampling errors, a statistical comparison is made against similar attributes measured from a suspect. A discrepancy index, C , is utilized as a measure of agreement between two samples that have N attributes measured. A threshold index, C_o , is selected at a percentage point of the χ^2 distribution for the associated N degrees of freedom. For $\alpha = 0.00001$, if $C > C_o$, then the probability that the samples came from different origins is 99.999%. The discrepancy index, C , is calculated by:

Table 1

Results of similarity analysis, values of D_i^2 indicated for each of the pairwise temperature comparisons for each attribute. No single attribute is sufficient for differentiation of all calcination temperatures. For $N = 1$, $C_o = 20$ for $\alpha = 0.00001$. For $N = 6$, $C_o = 34$ for $\alpha = 0.00001$. $C > C_o$ indicates a statistically significant difference at the 99.999% upper point of the χ^2 distribution.

Temperature comparison	Attribute						C, value
	Long needle ECD	Long needle minor ellipse	Surface grain ECD	Surface pore pixel area	Surface pore circularity	Amorph content	
350–400 °C	28.3	27.2	58.9	5.2	12.1	9.0	140.6
350–450 °C	9.6	1.3	32.5	54.2	3.3	87.1	188.1
350–500 °C	30.6	72.7	94.9	0.3	23.7	1906.4	2128.6
350–550 °C	323.4	291.5	32.8	111.7	72.1	6776.8	7608.4
400–450 °C	72.5	40.4	10.4	82.9	4.1	6.7	217.0
400–500 °C	113.8	169.5	8.5	5.3	3.2	424.5	724.7
400–550 °C	551.5	466.5	139.6	144.4	31.7	1110.9	2444.7
450–500 °C	6.8	57.5	36.5	23.4	13.7	630.7	768.6
450–550 °C	226.9	260.2	110.4	14.7	61.5	2075.6	2749.4
500–550 °C	137.9	49.4	178.1	56.1	12.2	328.0	761.8
Minimum, D_i^2	6.8	1.3	8.5	0.3	3.2	6.7	

$$C = \sum_{i=1}^N D_i^2 = \sum_{i=1}^N \left(\frac{(X_i - Y_i)}{(\sigma_{xi}^2 + \sigma_{yi}^2)^{1/2}} \right)^2 \tag{4}$$

where D_i^2 represents the square of the reduced difference for the i th attribute comparison, in which X_i and Y_i represent the measured attribute means for two compared samples, and σ_{xi} and σ_{yi} represent their respective standard errors.

The discrepancy index requires that the attributes investigated are normally distributed and not strongly correlated with one another. The various morphological area attributes were understandably strongly correlated with one another, and therefore only one area attribute was utilized for each feature type. The vector, convex hull, and ellipse perimeter values also showed strong correlation with the area attributes and were not utilized for comparison. The most successful uncorrelated discriminators, as determined by Tukey-Kramer honest significant difference testing [70,71], were included as an attribute for investigation by Parker's method. When coupled with the XRD-determined amorphous content, a total of 6 attributes were included for comparison.

The Shapiro-Wilk tests indicated that the selected quantitative morphological attribute data deviated significantly from a normal distribution [72]. Therefore, a univariate Box-Cox transformation was performed to transform each attribute data set to a normal distribution [73]. The transformations resulted in $\lambda = 0$ for the ECD (nm), minor ellipse length (nm), and pixel area (nm²). The circularity was transformed using $\lambda = 2$. To compare equal sample sizes, 500 morphological attribute data points were sampled from each calcination temperature. The results of the analysis using the 6 attributes for the demonstration

Table 2

Respective classification accuracies for the 350 °C and 400 °C training and testing set of SEM images.

350 °C vs 400 °C		
Classification iteration	Accuracy on training set	Accuracy on test set
1	95.3202%	90%
2	95.8128%	90%
3	95.0739%	90%
4	95.5665%	90%
5	95.5665%	90%
6	94.5813%	85%
7	94.3350%	90%
8	94.5813%	85%
9	94.0887%	95%
10	94.9507%	95%
Mean	94.9877%	90%
Std. Dev.	0.5807%	3.3333%

of calcination temperature differentiation can be seen below in Table 1.

The results indicate that no single attribute is sufficient to state that all the investigated temperatures are statistically different. This can be seen by comparing the minimum D_i^2 from each attribute against the critical value for a single attribute (i.e. $C_o = 20$ when $\alpha = 0.00001$). For six attributes, the critical value at the upper 99.999% point of the χ^2 distribution is $C_o = 34$. The combination of all six attributes allows for C to far exceed C_o at all pairwise compared temperatures. The amorphous content is a powerful discriminator when comparing the low and high temperature samples. The discrepancy index aligns intuitively with the expected deviation between samples as a function of calcination temperature. The greater the difference in the compared calcination temperatures, the greater the discrepancy index value. This analysis highlights the great advantage that multiple quantitative signatures can provide in differentiating samples.

3.6. Machine learning algorithm analysis

While quantitative analyses of multiple particle morphological features and the amorphous content proved an effective means of discriminating α - UO_3 according to the calcination history in the range of 350–550 °C, the complex and manually-intensive nature of these analyses leaves room for improvement. Often, nuclear materials analysis, especially for nuclear forensics, is time sensitive. The analysis above requires hundreds of person hours to complete. Nonetheless, it was visually apparent that there were stark differences between the SEM imaged morphologies of the various α - UO_3 calcination products. As noted previously, an appropriately trained multilayer neural network can excel at pattern recognition, potentially exceeding the capabilities of even a human observer. Therefore, in an effort to expedite the morphological analysis, machine learning was performed through a convolutional neural network for image classification of α - UO_3 by calcination temperature.

As a preliminary test of the efficacy of this method, four binary classifications were performed comparing 350 °C against 400, 450, 500, and 550 °C. Each binary classification was performed ten times. The final training and testing accuracies for the 350 °C vs 400 °C comparison can be seen in Table 2. All other comparisons can be seen in Tables A.23–A.25. The training accuracy evaluates discernment of the images based on calcination temperature from the same set of data used for training the network. The test accuracy is the ability to discern new images, not used for training, based on calcination temperature. Comparison of the SEM images acquired at 350 °C to those at the other individual calcination temperatures yielded a minimum average discernment of images based on temperature of $89.0 \pm 5.7\%$. The 350 °C vs 450 °C comparison resulted in the maximum average final testing accuracy of $94.0 \pm 2.1\%$. Hence, machine learning shows great

promise as a technique of the future for expediting image analysis in nuclear proliferomics.

4. Conclusion

The development of multiple nuclear material signatures within the framework of nuclear proliferomics has the potential to provide powerful new tools for nuclear material analysis. In this work, rather drastic morphological transformations were qualitatively presented for the calcination of unwashed uranyl peroxide at temperatures of 350, 400, 450, 500, and 550 °C. Through quantitative morphological analysis, it was shown that the morphology of any one surface feature present in the analyzed α - UO_3 samples was insufficient on its own to conclusively differentiate calcination temperature. Nonetheless, advanced statistical analysis coupling multiple morphological features with the x-ray diffraction spectra yielded complete discernment between the processing histories. Last, machine learning was applied to the analysis of the acquired SEM images to demonstrate their discernment with at least 89% accuracy. The methods provided open the door to a new field of study, nuclear proliferomics, which relies on the collection of vast libraries of data to identify signatures not readily available from standard nuclear forensics and nuclear safeguard analysis tools.

Acknowledgements

This synthesis of α - UO_3 and their subsequent characterization by p-XRD, SEM, TGAMS, and DSC was supported by the U.S. Department of Homeland Security, Domestic Nuclear Detection Office, under Grant Award no. 2015-DN-077-ARI092. The same DHS grant, along with the Defense Threat Reduction Agency, under Grant Award no. HDTRA1-16-1-0026 supported the quantitative analysis via MAMA. The machine learning analysis was supported by the U.S. Department of Homeland Security, Domestic Nuclear Detection Office, under Grant Award no. 2016-DN-077-ARI102. The views and conclusions contained in this document are those of the authors and should not be interpreted as necessarily representing the official policies, either expressed or implied, of the U.S. Department of Homeland Security or Defense Threat Reduction Agency.

This work made use of University of Utah Shared facilities of the Surface Analysis and Nanoscale Imaging Group sponsored by the College of Engineering, Health Sciences Center, Office of the Vice President for Research, and the Utah Science Technology and Research (USTAR) Initiative of the State of Utah. This work made use of the Materials Characterization Lab at the University of Utah. The authors would like to thank Dana W. Overacker for providing invaluable assistance with the TGA-MS equipment and Dr. Taylor Sparks for his insights on quantitative p-XRD analysis. The authors would also like to thank Dr. Sue B. Clark for her insightful discussions of analytical techniques and nuclear material processing.

Appendix A. Supplementary material

Supplementary data associated with this article can be found in the online version at <http://dx.doi.org/10.1016/j.talanta.2018.04.092>.

References

- [1] S. Niemeyer, D.K. Smith, The Role of Nuclear Forensics in Preventing Nuclear Terrorism, Lawrence Livermore National Laboratory (LLNL), Livermore, CA, 2007.
- [2] L. Gil, The deterrent effect of nuclear forensics: the case of Hungary, *IAEA Bull.* 57 (4) (2016) 8–11 (Online).
- [3] Y. Jeong, J.J. Han, S. Chang, H.W. Shim, S. Ahn, Study on interface between nuclear material accounting system and national nuclear forensic library, KNS 2016 Autumn Meeting, 2016.
- [4] R.P. Horgan, L.C. Kenny, 'Omic' technologies: genomics, transcriptomics, proteomics and metabolomics, *Obstet. Gynaecol.* 13 (3) (2011) 189–195.
- [5] K. Song, J.-H. Park, C.-G. Lee, S.-H. Han, Recent developments in nuclear forensic and nuclear safeguards analysis using mass spectrometry, *Mass Spectrom. Lett.* 7 (2) (2016) 31–40.
- [6] T.L. Spano, A. Simonetti, E. Balboni, C. Dorais, P.C. Burns, Trace element and U isotope analysis of uraninite and ore concentrate: applications for nuclear forensic investigations, *Appl. Geochem.* 84 (2017) 277–285.
- [7] L.W. McDonald IV, J.A. Campbell, T. Vercouter, S.B. Clark, Characterization of actinides complexed to nuclear fuel constituents using ESI-MS, *Anal. Chem.* 88 (5) (2016) 2614–2621.
- [8] I.J. Schwerdt, A. Olsen, R. Lusk, S. Heffernan, M. Klosterman, B. Collins, S. Martinson, T. Kirkham, L.W. McDonald, Nuclear forensics investigation of morphological signatures in the thermal decomposition of uranyl peroxide, *Talanta* 176 (Suppl. C) (2018) S284–S292.
- [9] D. Reilly, N. Ensslin, H. Smith Jr, S. Kreiner, Passive nondestructive assay of nuclear materials, Nuclear Regulatory Commission, Washington, DC, United States. Office of Nuclear Regulatory Research; Los Alamos National Lab., NM, United States, 1991.
- [10] G.L. Klunder, J.W. Plaupe, P.E. Spackman, P.M. Grant, R.E. Lindvall, I.D. Hutcheon, Application of visible/near-infrared reflectance spectroscopy to uranium ore concentrates for nuclear forensic analysis and attribution, *Appl. Spectrosc.* 67 (9) (2013) 1049–1056.
- [11] T.G. Ditcham, A. Wotherspoon, K.P. Kirkbride, C.E. Lenehan, R.S. Popelka-Filcoff, Thermal decomposition of Australian uranium ore concentrates: characterisation of speciation and morphological changes following thermogravimetric analysis, *J. Radioanal. Nucl. Chem.* 310 (2) (2016) 725–732.
- [12] D.M. Hausen, Characterizing and classifying uranium yellow cakes: a background, *JOM* 50 (12) (1998) 45.
- [13] L. Käll, J.D. Canterbury, J. Weston, W.S. Noble, M.J. MacCoss, Semi-supervised learning for peptide identification from shotgun proteomics datasets, *Nat. Methods* 4 (11) (2007) 923–925.
- [14] K. Kourou, T.P. Exarchos, K.P. Exarchos, M.V. Karamouzis, D.I. Fotiadis, Machine learning applications in cancer prognosis and prediction, *Comput. Struct. Biotechnol. J.* 13 (2015) 8–17.
- [15] M.W. Libbrecht, W.S. Noble, Machine learning applications in genetics and genomics, *Nat. Rev. Genet.* 16 (6) (2015) 321–332.
- [16] R. Porter, N. Harvey, C. Ruggiero, Investigation of segmentation based pooling for image quantification, *Proc. SPIE-IS&T* 9024 (2014) 90240F–90241F.
- [17] R. Porter, C. Ruggiero, D. Hush, N. Harvey, P. Kelly, W. Scoggins, L. Tandon, Interactive image quantification tools in nuclear material forensics, *Proc. SPIE* (2011) 787708–787708-9.
- [18] A.E. Jones, P. Turner, C. Zimmerman, J.Y. Goulermas, Classification of spent reactor fuel for nuclear forensics, *Anal. Chem.* 86 (11) (2014) 5399–5405.
- [19] A. Jones, A. Keatley, J. Goulermas, T. Scott, P. Turner, R. Awbery, M. Stapleton, Machine learning techniques to repurpose uranium ore concentrate (UOC) industrial records and their application to nuclear forensic investigation, *Appl. Geochem.* (2017).
- [20] K. Luetzenkirchen, K. Mayer, How a database of nuclear databases could help the effort to combat trafficking, *Nature* 445 (7125) (2007) (256–256).
- [21] K. Mayer, Security: expand nuclear forensics, *Nat. News* 503 (7477) (2013) 461.
- [22] E.H.P. Cordfunke, A.A. Van Der Giessen, Pseudomorphic decomposition of uranium peroxide into UO_3 , *J. Inorg. Nucl. Chem.* 25 (5) (1963) 553–555.
- [23] A.M. Olsen, B. Richards, I. Schwerdt, S. Heffernan, R. Lusk, B. Smith, E. Jurrus, C. Ruggiero, L.W. McDonald, Quantifying morphological features of α - U_3O_8 with image analysis for nuclear forensics, *Anal. Chem.* 89 (5) (2017) 3177–3183.
- [24] E. Kümmerle, G. Heger, The structures of $\text{C-Ce}_2\text{O}_3$, Ce_7O_{12} , and $\text{Ce}_{11}\text{O}_{20}$, *J. Solid State Chem.* 147 (2) (1999) 485–500.
- [25] T. Degen, M. Sadki, E. Bron, U. König, G. Nénert, The highscore suite, *Powder Diffraction* 29 (2) (2014) S13–S18.
- [26] ICDD, PDF-2 database release 2008, International Centre for Diffraction Data (ICDD), 2008.
- [27] P.F. Weck, E. Kim, C.F. Jové-Colón, D.C. Sassani, Structures of uranyl peroxide hydrates: a first-principles study of studtite and metastudtite, *Dalton Trans.* 41 (32) (2012) 9748–9752.
- [28] A. Eaton, L. Clesceri, E. Rice, A. Greenberg, M. Franson, Standard Methods for the Examination of Water and Wastewater 21 American Public Health Association, Washington, DC, 2005.
- [29] Y. LeCun, L. Bottou, Y. Bengio, P. Haffner, Gradient-based learning applied to document recognition, *Proc. IEEE* 86 (11) (1998) 2278–2324.
- [30] K. Simonyan, A. Zisserman, Very deep convolutional networks for large-scale image recognition, arXiv preprint arXiv:1409.1556, 2014.
- [31] M. Abadi, P. Barham, J. Chen, Z. Chen, A. Davis, J. Dean, M. Devin, S. Ghemawat, G. Irving, M. Isard, TensorFlow: A System for Large-Scale Machine Learning, OSDI, 2016, pp. 265–283.
- [32] I. TheMathworks, MATLAB and Statistics Toolbox Release 2017a, Natick, Massachusetts, United States, 2017.
- [33] J.R. Sanderson, H.E. Dibben, H. Mason, The reaction between hydrogen peroxide and solutions of pure uranyl salts. Part I: the interaction of hydrogen peroxide and uranyl nitrate, United Kingdom, 1951.
- [34] W.H. Smith, Thermal dehydration of uranyl nitrate hydrates, *J. Inorg. Nucl. Chem.* 30 (7) (1968) 1761–1768.
- [35] S. Dash, M. Kamruddin, S. Bera, P.K. Ajikumar, A.K. Tyagi, S.V. Narasimhan, B. Raj, Temperature programmed decomposition of uranyl nitrate hexahydrate, *J. Nucl. Mater.* 264 (3) (1999) 271–282.
- [36] J.R. Bridge, C.W. Melton, C.M. Schwartz, D.A. Vaughan, Thermal Decomposition of Uranyl Nitrate Hexahydrate, Battelle Memorial Institute, 1956 USAEC Report BMI-1110.
- [37] T.J. Johnson, L.E. Sweet, D.E. Meier, E.J. Mausolf, E. Kim, P.F. Weck, E.C. Buck, B.K. McNamara, Time-resolved infrared reflectance studies of the dehydration-

- induced transformation of uranyl nitrate hexahydrate to the trihydrate form, *J. Phys. Chem. A* 119 (39) (2015) 9996–10006.
- [38] K.E. Knope, L. Soderholm, Solution and solid-state structural chemistry of actinide hydrates and their hydrolysis and condensation products, *Chem. Rev.* 113 (2) (2013) 944–994.
- [39] L.R. Morss, N.M. Edelstein, J. Fuger, J.J. Katz, *The Chemistry of the Actinide and Transactinide Elements*, 4th ed., Springer, Dordrecht, 2011.
- [40] J.L. Woodhead, A.M. Deane, A.C. Fox, J.M. Fletcher, The preparation and properties of a polynuclear uranyl nitrate, *J. Inorg. Nucl. Chem.* 28 (10) (1966) 2175–2185.
- [41] M. Aberg, The crystal structure of Hexaqua-tri-a—hydroxo—a3-oxo-triuranyl (VI) nitrate tetrahydrate, *Acta Chem. Scand. A* 32 (2) (1978).
- [42] S. Kulyukhin, A. Kamenskaya, I. Rumer, Mechanism of $\text{UO}_2(\text{NO}_3)_2 \cdot 6\text{H}_2\text{O}$ decomposition under the action of microwave radiation: Part 2, *Radiochemistry* 51 (5) (2009) 469.
- [43] E. Cordfunke, The system $\text{UO}_2(\text{NO}_3)_2 \cdot \text{UO}_3 \cdot \text{H}_2\text{O}$, *J. Inorg. Nucl. Chem.* 34 (2) (1972) 531–534.
- [44] K.V. Rajagopalan, P.V. Ravindran, T.P. Radhakrishnan, Thermal decomposition of uranyl nitrate hexahydrate, *J. Therm. Anal.* 44 (1) (1995) 89–96.
- [45] E.H.P. Cordfunke, *The Chemistry of Uranium: Including its Applications in Nuclear Technology*, Elsevier Pub. Co., London, Amsterdam, New York, 1970.
- [46] R.D. Kozlova, V.A. Matyukha, N.V. Dedov, Mechanism and kinetics of thermal decomposition of uranyl nitrate hexahydrate under the nonisothermal conditions, *Radiochemistry* 49 (2) (2007) 130–134.
- [47] R.S. Ondrejcin, Thermal denitration of uranyl nitrate hexahydrate, *J. Chem. Eng. Data* 11 (1) (1966) 130–133.
- [48] B. Kalekar, N. Rajee, A. Reddy, Solid state interaction studies on binary nitrate mixtures of uranyl nitrate hexahydrate and lanthanum nitrate hexahydrate at elevated temperatures, *J. Nucl. Mater.* 484 (2017) 16–23.
- [49] X. Guo, D. Wu, H. Xu, P.C. Burns, A. Navrotsky, Thermodynamic studies of studdite thermal decomposition pathways via amorphous intermediates UO_3 , U_2O_7 , and UO_4 , *J. Nucl. Mater.* 478 (2016) 158–163.
- [50] S.O. Odoh, J. Shamblin, C.A. Colla, S. Hickam, H.L. Lobeck, R.A. Lopez, T. Olds, J.E. Szymanowski, G.E. Sigmon, J. Neufeind, W.H. Casey, M. Lang, L. Gagliardi, P.C. Burns, Structure and reactivity of X-ray amorphous uranyl peroxide, U_2O_7 , *Inorg. Chem.* 55 (7) (2016) 3541–3546.
- [51] T. Sato, Thermal decomposition of uranium peroxide hydrates, *J. Appl. Chem. Biotechnol.* 26 (4) (1976) 207–213.
- [52] R. Thomas, M. Rivenet, E. Berrier, I. de Waele, M. Arab, D. Amaraggi, B. Morel, F. Abraham, Thermal decomposition of $(\text{UO}_2)_2(\text{H}_2\text{O})_2 \cdot 2\text{H}_2\text{O}$: influence on structure, microstructure and hydrofluorination, *J. Nucl. Mater.* 483 (2017) 149–157.
- [53] K.W. Kim, J.T. Hyun, K.Y. Lee, E.H. Lee, K.W. Lee, K.C. Song, J.K. Moon, Effects of the different conditions of uranyl and hydrogen peroxide solutions on the behavior of the uranium peroxide precipitation, *J. Hazard. Mater.* 193 (2011) 52–58.
- [54] A.L. Tamasi, L.J. Cash, C. Eley, R.B. Porter, D.L. Pugmire, A.R. Ross, C.E. Ruggiero, L. Tandon, G.L. Wagner, J.R. Walensky, A.D. Wall, M.P. Wilkerson, A lexicon for consistent description of material images for nuclear forensics, *J. Radioanal. Nucl. Chem.* 307 (3) (2016) 1611–1619.
- [55] A.L. Tamasi, L.J. Cash, W. Tyler Mullen, A.R. Ross, C.E. Ruggiero, B.L. Scott, G.L. Wagner, J.R. Walensky, S.A. Zerkle, M.P. Wilkerson, Comparison of morphologies of a uranyl peroxide precursor and calcination products, *J. Radioanal. Nucl. Chem.* (2016).
- [56] H.-D. Yu, Z.-Y. Zhang, K.Y. Win, J. Chan, S.H. Teoh, M.-Y. Han, Bioinspired fabrication of 3D hierarchical porous nanostructures of calcium carbonate for bone regeneration, *Chem. Commun.* 46 (35) (2010) 6578–6580.
- [57] C.E. Ruggiero, R.B. Porter, *MAMA Software Features: Quantified Attributes*, Los Alamos National Laboratory, Los Alamos, NM, 2014.
- [58] R. Jenkins, R.L. Snyder, *Introduction to X-ray powder diffractometry*, Chemical Analysis, A Series of Monographs on Analytical Chemistry and its Applications, 138 Wiley, New York, 1996.
- [59] V.K. Pecharsky, P.Y. Zavalij, *Fundamentals of Powder Diffraction and Structural Characterization of Materials*, Springer, New York, NY, 2009.
- [60] I.C. Madsen, N.V. Scarlett, A. Kern, Description and survey of methodologies for the determination of amorphous content via X-ray powder diffraction, *Z. für Krist. Cryst. Mater.* 226 (12) (2011) 944–955.
- [61] H. Rietveld, A profile refinement method for nuclear and magnetic structures, *J. Appl. Crystallogr.* 2 (2) (1969) 65–71.
- [62] D.L. Bish, S. Howard, Quantitative phase analysis using the Rietveld method, *J. Appl. Crystallogr.* 21 (2) (1988) 86–91.
- [63] B.M. Pederson, K.J. Schaible, R.S. Winburn, *Minimization of Errors Due to Microabsorption or Absorption Contrast*, (2004).
- [64] G.W. Brindley, XLV. The effect of grain or particle size on X-ray reflections from mixed powders and alloys, considered in relation to the quantitative determination of crystalline substances by X-ray methods, *Lond. Edinb. Phil. Mag. J. Sci.* 36 (256) (1945) 347–369.
- [65] A. Tsvignunov, L. Kuznetsov, On the type of $\alpha\text{-UO}_3$ superstructure, *Radiokhimiya* 21 (5) (1979) 747–753.
- [66] K. Naito, K. Kamegashira, C.-K. Furo-Cho, High temperature chemistry of ceramic nuclear fuels with emphasis on non-stoichiometry, *Adv. Nucl. Sci. Technol.* 9 (1976) 99–180.
- [67] J. Parker, A statistical treatment of identification problems, *J. Forensic Sci. Soc.* 6 (1) (1966) 33–39.
- [68] J. Parker, The mathematical evaluation of numerical evidence, *J. Forensic Sci. Soc.* 7 (3) (1967) 134–144.
- [69] J. Parker, A. Holford, Optimum test statistics with particular reference to a forensic science problem, *Appl. Stat.* (1968) 237–251.
- [70] C.Y. Kramer, Extension of multiple range tests to group means with unequal numbers of replications, *Biometrics* 12 (3) (1956) 307–310.
- [71] J.W. Tukey, The problem of multiple comparisons, *Mult. Comp.* (1953).
- [72] S.S. Shapiro, M.B. Wilk, An analysis of variance test for normality (complete samples), *Biometrika* 52 (3/4) (1965) 591–611.
- [73] G.E. Box, D.R. Cox, An analysis of transformations, *J. R. Stat. Soc. Ser. B (Methodol.)* (1964) 211–252.